Theoretical and Applied Fracture Mechanics 116 (2021) 103120

Contents lists available at ScienceDirect

Theoretical and Applied Fracture Mechanics

journal homepage: www.elsevier.com/locate/tafmec

Size-effect on the apparent tensile strength of brittle materials with spherical cavities

A. Chao Correas *, M. Corrado, A. Sapora, P. Cornetti

Department of Structural, Geotechnical and Building Engineering, Politecnico di Torino, Corso Duca degli Abruzzi 24, 10129 Torino, Italy

ARTICLE INFO

Keywords:
Spherical cavity
Size effect
Quasi-brittle materials
Finite Fracture Mechanics
Cohesive Zone Model
Theory of Critical Distances

ABSTRACT

The decrease of the apparent uniaxial tensile strength resulting from a single flawless spherical cavity in an infinite linear elastic continuum under uniaxial tension is investigated. To this end, a new generalized semi-analytical expression for the stress intensity factor of an annular crack surrounding the spherical cavity under different loading conditions is proposed and validated. The apparent tensile strength is then estimated by four different approaches: two criteria implement a single condition, either on the stress field (Theory of Critical Distances) or on the energy release rate (equivalent Linear Elastic Fracture Mechanics), whereas the other two are stress-energy coupled criteria, namely the Finite Fracture Mechanics and the Cohesive Zone Model. Finally, theoretical predictions are discussed and compared with experimental data and atomistic simulations available in the literature, showing good correlation.

1. Introduction

The use of brittle materials for critical structural components has been largely limited by the strong flaw-sensitiveness of their failure behavior, which introduces a stochastic uncertainty in the effective strength, thus increasing its unreliability and making them difficult to characterize. Nonetheless, certain materials that fall within this category, e.g. ceramics and glass, present some other characteristics, such as heat and wear resistance or chemical inertness, that make them strong candidates for structural applications in extreme environments. Therefore, the research activity on the effect that different flaws and their size have on the ultimate behavior is of paramount importance to ensure the safe use of brittle materials.

This paper focuses on flaws whose shape is (or can be approximated as) spherical. The effect of the spherical void's size and the related material porosity on the structural strength of brittle materials has been considered in experimental studies, such as those in [1] on borosilicate glass and in [2] on alumina composites. Therein it was found that, for pores big enough, even very low porosities had a noticeable reductive effect on the strength (up to 50%). Likewise, this dependence clearly showcased a size effect, since the weakening diminished with decreasing pore size, meaning that simple strength predictions based on the stress concentration factor derived in [3] are not reliable. Similar size effects were experimentally observed on single voided silicon nitride specimens in [4] and in the atomistic simulations of silicon carbide in [5].

However, this size effect on the weakening of "defective" specimens is not particular to those having spherical pores, but in general to any kind of defect resulting in a stress concentration. It is well known (see e.g. [6]) that the size effect on the strength of brittle or quasi-brittle materials can be caught by introducing energetic considerations into stress-based failure criteria. Following this thread, different failure criteria have incorporated energy-related magnitudes in their formulation: either explicitly, such as Finite Fracture Mechanics (FFM) or Cohesive Zone Model (CZM); implicitly, through a fixed length depending on the fracture toughness, as the Theory of Critical Distances (TCD); or have extended the conventional Linear Elastic Fracture Mechanics for its use in uncracked bodies like the equivalent LEFM (eqLEFM). Referring specifically to FFM, previous studies have successfully predicted either analytically or semi-analytically the scaling of structural strength for both singular and non-singular elemental geometries. To cite but a few, here there can be quoted a slab with a through-thickness crack [7,8], a solid with a Penny-shaped crack [9], a plate with a circular hole [10–13] and plain and notched specimens under three-point bending [14,15].

Abbreviations: FFM, Finite Fracture Mechanics; CZM, Cohesive Zone Model; TCD, Theory of Critical Distances; LEFM, Linear Elastic Fracture Mechanics; eqLEFM, Equivalent Linear Elastic Fracture Mechanics; avg, Average; PM, Point Method; LM, Line Method; SIF, Stress Intensity Factor; SERR, Strain Energy Release Rate; CMOD, Crack Mouth Opening Displacement; URS, Uniform Remote Stress (loading); CSL, Constant Stress Lip (loading); LLE, Line-Load Edge (loading).

* Corresponding author.
E-mail address: arturo.chaocorreas@polito.it (A. Chao Correas).

https://doi.org/10.1016/j.tafmec.2021.103120
Received 7 July 2021; Received in revised form 16 September 2021; Accepted 30 September 2021
Available online 4 October 2021

Nomenclature

(r,θ,z)	Cylindrical coordinates triad
R	Spherical void's radius
a	Annular crack radial length
E	Young's modulus
ν	Poisson's ratio
σ_{zz}	Normal stress component as per z
σ_∞	Uniform remote stress
σ_c	Unvoided strength/Cohesive stress
$\overline{P}$	Line-load
K_I	Stress intensity factor
β	Interpolation function
F^{σ_i}	Geometric shape function under stress $\sigma_i (i = \{\infty, c\})$ loadings
$F^{\overline{P}}$	Geometric shape function under line-load $\overline{P}$ conditions
$u_z^{\sigma_i}(R,0)$	Crack mouth opening displacement under $\sigma_i (i = \{\infty, c\})$ loadings
σ_f	Failure stress
Δ	Finite crack extension
a_p	Process zone radial length
l_{ch}	Irwin's length
K_{Ic}	Fracture toughness

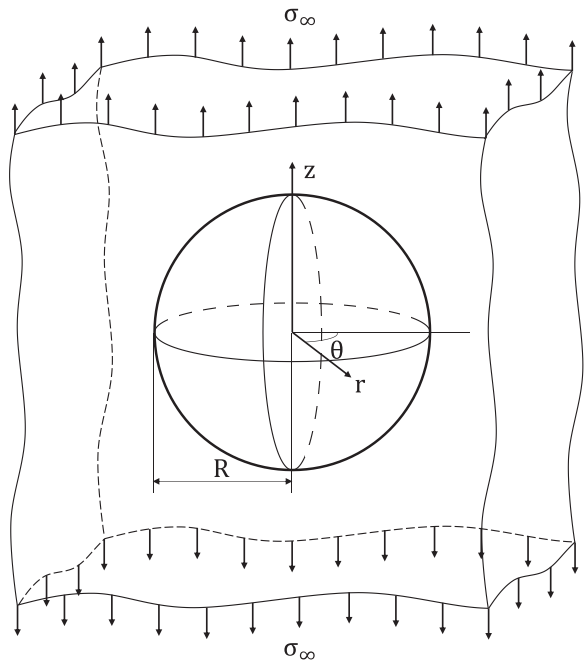

Fig. 1. Schematic representation of a spherical void in an infinite tensioned body in 3D.

However, to the author's best knowledge, no study has so far faced the strength size effect of specimens containing spherical voids by means of the previously mentioned approaches. Some relevant studies on the topic include the work in [16], which was based on Weibull statistical analysis, or those in [17,18], where LEFM was used by assuming the presence of an annular crack surrounding the void.

Therefore, given the representativeness showcased by the already mentioned coupled (stress and energy) failure criteria, the present work will focus on their particularization to the problem herein considered. The required analytical expressions for the stress field and Stress Intensity Factor are provided in Section 2. Making use of these relations, the failure predictions by Finite Fracture Mechanics, Cohesive Zone Model and other relevant methods are given in Sections 3, 4 and 5 respectively, in a semi-analytical fashion. Eventually, comparisons against experimental results and atomistic simulations available in the literature are shown in Section 6, and the final conclusions are drawn in Section 7.

2. The annular crack around a spherical void

Should a single spherical void of radius R be present in an otherwise solid infinite domain tensioned in the z-direction by a constant remote stress σ_∞ (as in Fig. 1) the elsewhere uniaxial and uniform stress field is perturbed in the surroundings of the feature. If the domain is filled with a homogeneous and isotropic material, fracture is expected to occur as a mode I annular crack stemming from the void's equator (hereafter annular crack) and lying in the $z = 0$ plane. On such a plane, the normal stress is given by Eq. (1) according to [3]. Hence, the stress concentration factor is as in Eq. (2), varying from 1.93 to 2.17 as the Poisson's ratio ν changes from 0 to 0.5; noteworthy, it is equal to 2 for $\nu = 0.2$.

$$\sigma_{zz}(r,\theta,0) = \sigma_\infty \left[1 + \frac{4-5\nu}{2(7-5\nu)}\left(\frac{R}{r}\right)^3 + \frac{9}{2(7-5\nu)}\left(\frac{R}{r}\right)^5\right] \tag{1}$$

$$\frac{\sigma_{zz}(R,\theta,0)}{\sigma_\infty} = \frac{3(9-5\nu)}{2(7-5\nu)} \tag{2}$$

As evident from Eqs. (1) and (2), and differently from what happens around a circular hole (see [19]), there exists a dependency on the Poisson's ratio ν and, thus, the stress field is material dependent. In what follows, unless otherwise specified, ν will be taken equal to 0.2.

No dependence on the azimuth angle θ is noted in geometry, loading or material properties. Since also the crack onset is assumed to share the same feature, the problem is to be treated as axisymmetric onwards, reducing the tridimensional system of coordinates (r, θ, z) to a bidimensional one as (r,z).

In the following, the annular crack onset will be tackled, among other approaches, by means of FFM and CZM. To this aim, the expressions for both the Stress Intensity Factor (SIF) and the Crack Mouth Opening Displacement (CMOD) for different loading cases are needed, although exact definitions for any of these magnitudes are not achievable. On the other hand, accurate approximate solutions can still be obtained on the basis that an annular crack of radial length a surrounding the spherical void of radius R respectively resembles an Edge-Crack (EC) or a Penny-shaped Crack (PC) in the limits $a/R \to 0$ and $a/R \to \infty$. Based upon these tendencies, Fett [20] proposed that the approximate solution for the annular crack can be obtained through an interpolation based on these two known limit cases.

In the following subsection, a generalized approximate analytical expression of the annular crack's SIF, along with its particularizations to different loading cases, is provided by exploiting a procedure similar to the one proposed in [20], but improving the expression's simplicity and robustness.

2.1. Stress Intensity Factors

In order to apply FFM, one needs the SIF for the annular crack loaded by a Uniform Remote Stress (σ_∞ – URS); to apply the CZM, also those for the Constant-Stress Lip (σ_c – CSL) loading and the Line-Load Edge ($\overline{P}$ – LLE) scenarios are necessary. A schematic description of each of these loading cases is found in Fig. 2 (a), (b) and (c), respectively.

For the URS and CSL loading cases, the general structure of the SIF's expressions proposed in [20] was as in Eq. (3), where the interpolation function $\beta_{Fett}(a,R)$ was always kept as shown in Eq. (4). In said reference, only the proposal for the URS's SIF expression was proven to be in close agreement with results from the literature, while no proof on the

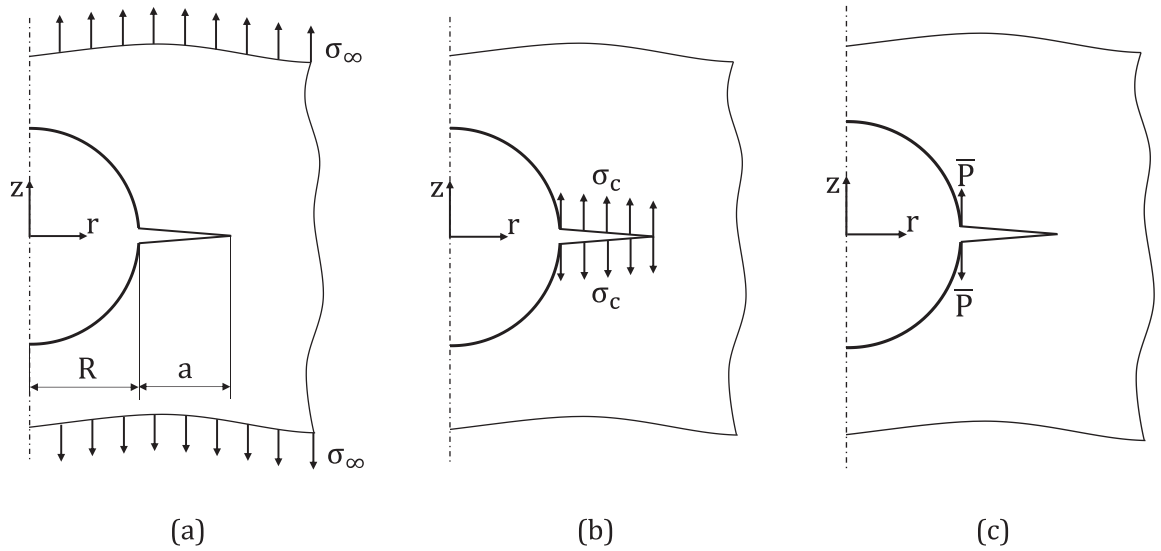

Fig. 2. Schematic representation of the considered loadings: (a) URS; (b) CSL; and (c) LLE.

accuracy of the therein proposed CSL's SIF function was provided. Likewise, the LLE loading case was not addressed.

$$K_I = \left[K_I^{PC} + \left(K_I^{EC}\big|_{a/R\to 0} - K_I^{PC}\big|_{a/R\to 0}\right)\right] \beta_{Fett}(a,R) + K_I^{PC}\ [1-\beta_{Fett}(a,R)\,] \tag{3}$$

$$\beta_{Fett}(a,R) = \left(\frac{R}{R+2a}\right)^2 \tag{4}$$

Therefore, given the complexity of the expression in Eq. (3), added to the lack of proof of this proposal's applicability for two out of the three required cases, it is herein introduced in Eq. (5) a new generalized (and simpler) expression for the SIF of an annular crack under different loading conditions, where the new interpolation function $\beta(a,R)$ is that in Eq. (6).

$$K_I = K_I^{EC}\ \beta(a,R) + K_I^{PC}\ [1-\beta(a,R)\,] \tag{5}$$

$$\beta(a,R) = \left(\frac{R}{R+ma}\right)^2 \tag{6}$$

Eq. (5) still relies on the same basic idea used in relevant former studies such as [20] and [21]: the annular crack's SIF may be approximated by combining the solutions of known simpler cases. Nonetheless, Eq. (5) shows in a clearer way with respect to Eq. (3) that the proposed annular crack SIF function is obtained through a weighted sum of the respective Edge Crack's and Penny-shaped Crack's SIF solutions.

On the other hand, the interpolation function in Eq. (6) coincides with the one in Eq. (4) except for the strictly positive parameter m, which, for the sake of generality and robustness, is now left to be independently defined for each loading case. Of course, the interpolation function always fulfils the extreme cases since $\beta\to 1$ for $a/R\to 0$, and $\beta\to 0$ as $a/R\to\infty$. Besides, the values of m subsequently particularized in this subchapter were chosen for each addressed loading scenario to deliver accurate results against the respective numerical simulations and results from the literature, as it will be then shown in Section 2.3.

According to Eq. (5), the SIF of the annular crack only depends on the respective solutions for both the Edge Crack and Penny-shaped Crack under the corresponding crack-plane stress distributions defined by $\sigma_{zz}(r)$. For simple loading cases, these SIF functions are known. To further simplify the formulation, the component K_I^{EC}, having only a relevant effect on the solution when $a/R\to 0$, is onwards replaced by its limit value $K_I^{EC}\big|_{a/R\to 0}$. This assumption allows computing the otherwise complex SIF solution of the Edge Crack under the URS loading case as if it was loaded by constant normal stress equal to $\sigma_\infty\ [(27-15\nu)/(14-10\nu)\,]$ (see Eq. (2)).

With regards to using non-dimensional magnitudes for subsequent comparisons, it is introduced in Eq. (7) the SIF geometric shape function relative to the i-th loading case (F^{σ_i}), where $\sigma_i (i=\{\infty,c\}\,)$ stands for the characteristic stress of either the URS (σ_∞) or the CSL (σ_c) cases.

$$K_I^{\sigma_i} = \sigma_i\sqrt{\pi a}F^{\sigma_i} \tag{7}$$

Instead, for the LLE ($\overline{P}$) scenario the SIF geometric shape function is as in Eq. (8).

$$K_I^{\overline{P}} = \frac{\overline{P}}{\sqrt{\pi a}}F^{\overline{P}} \tag{8}$$

Subsequently, Eq. (9) is the proposal of the SIF geometric shape function for the URS case, obtained from Eqs. (5) and (7) by setting $m=5$. The Penny-shaped Crack solution is obtained via the weight function method as described in [20] and making use of the stress $\sigma_{zz}(r)$ in Eq. (1), while that of the Edge Crack is the well-known 1.122 factor times the void's stress concentration.

$$F^{\sigma_\infty}(a,R,\nu) = 1.122\ \frac{27-15\nu}{14-10\nu}\left(\frac{R}{R+5a}\right)^2 + \frac{2}{\pi}\sqrt{\frac{a+2R}{a+R}}\cdot \left[1+\frac{R^2}{2(a+R)^2}+\frac{3R^4}{(7-5\nu)(a+R)^4}\right]\left[1-\left(\frac{R}{R+5a}\right)^2\right] \tag{9}$$

For the LLE scenario, Eqs. (5) and (8) yield the SIF geometric shape function in Eq. (10) when $m=5$. Here, the solutions for the Edge and Penny-shaped Cracks are taken from [22].

$$F^{\overline{P}}(a,R) = 2{\cdot}1.297\left(\frac{R}{R+5a}\right)^2 + \frac{2R}{\sqrt{(a+R)(a+2R)}}\left[1-\left(\frac{R}{R+5a}\right)^2\right] \tag{10}$$

Eventually, by now using $m=2$, the particularization of Eqs. (5) and (7) results into the CSL's SIF geometric shape function in Eq. (11), which exactly coincides with that proposed in [20]. Again, the solutions for the limit cases (Edge Crack and Penny-shaped Crack) are obtained from [22].

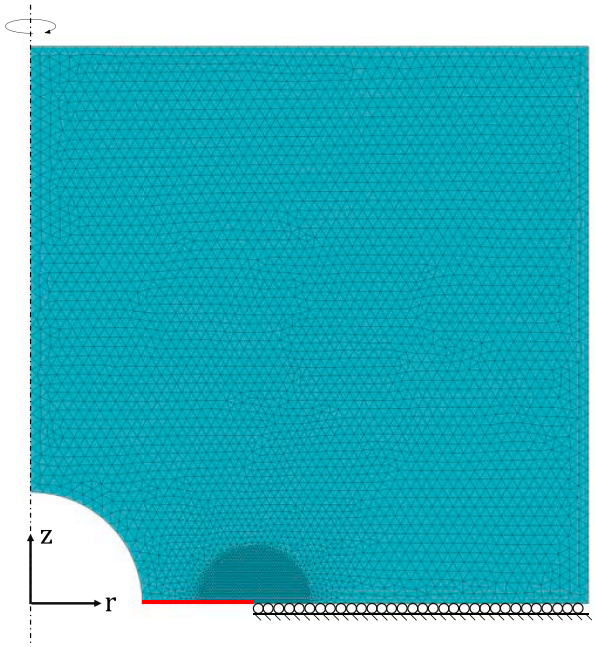

Fig. 3. Schematic representation of the mesh definition and boundary conditions for the Finite Element model with a ratio $a/R = 1$. Crack highlighted in red. (For interpretation of the references to colour in this figure legend, the reader is referred to the web version of this article.)

$$F^{\sigma_c}(a,R) = 1.122\left(\frac{R}{R+2a}\right)^2 + \frac{2}{\pi}\sqrt{\frac{a+2R}{a+R}}\left[1-\left(\frac{R}{R+2a}\right)^2\right] \tag{11}$$

2.2. Crack Mouth opening displacement (CMOD)

Paris' integral, introduced in [23], relates the CMOD of a loading condition (σ_i) to the SIF functions of the very same scenario of interest plus an auxiliary one (LLE-$\overline{P}$). For the axisymmetric case at hand, this equation reads as in Eq. (12).

$$u_z^{\sigma_i}(R,0) = \frac{(1-\nu^2)}{E}\int_0^a K_I^{\sigma_i}\frac{\partial K_I^{\overline{P}}}{\partial \overline{P}}\frac{R+a'}{R}\mathrm{d}a' \tag{12}$$

Subsequently, Eq. (12) allows to indirectly verify the herein proposed analytical interpolating expressions through the CMODs obtained via Finite Element analyses, which, as is well known, can deliver very accurate results for the displacement field far from the singularity.

2.3. Finite Element model

Throughout this section, the Finite Element analyses used to check the shape functions proposed in Eqs. (9)–(11) is detailed. The axisymmetric linear elastic model was developed using FEniCS [24] in a Python environment. The mathematical operators required for the solving and post-processing were those of the Unified Form Language library, whereas the meshing operations were based on the GMSH library. Combining these open-source libraries allows the development of high-performance numerical codes for variational problems.

Since the studied problem is axisymmetric, the considered integration domain Ω for the variational formulation is bidimensional and defined in the (r, z) space whereas both its boundary $\partial\Omega$ and the geometrical locus of the crack Γ are one-dimensional. The displacement field $\vec{u}$ is regarded as a tridimensional vectorial function with only non-zero components as per $\vec{e}_r$ and $\vec{e}_z$ directions. The stress $\overline{\sigma}$ and strain $\overline{\varepsilon}$ tensors are also tridimensional, as the hoop components are not zero. Moreover, it is worth reminding that the integral operators for area and curve integrals are respectively $\mathrm{d}\vec{x} = r\,\mathrm{d}r\,\mathrm{d}z$ and $\mathrm{d}\varsigma = r\,\mathrm{d}s$ when cylindrical coordinates are used, and that the axisymmetric condition imposes that $\partial(\cdot)/\partial\theta = 0$.

The hypothesis of infinite solid domain surrounding the void stated above is reasonably relaxed to that of considering a sufficiently large domain with respect to the void and crack characteristic lengths, so that the free-edge effects are negligible. Then, the domain is discretized with first-order triangular elements, since an increase of the element order does not increase the accuracy, for cracked solids and in terms of the energy norm, of the approximate solution $\vec{u}^h$ with respect to the exact one $\vec{u}$. Moreover, as only the reduction in the characteristic mesh size is proven useful to reduce the error of the Finite Element approximation, mesh refinement is imposed close to the crack tip so that the element size is fifty times smaller than the crack length, as schematically shown in Fig. 3. The accuracy of this discretization is assessed with an auxiliary dual model of a Penny-shaped Crack, for which the analytical SIF solution is known, being its relative error below 1.5%. Externally applied stresses are as in Fig. 2 (a) or (b) for the URS and CSL loading cases, respectively. Moreover, the vertical symmetry of the problem is exploited, so that just one half of the axisymmetric domain is modeled.

Subsequently, the resolution of the variational problem with the respective boundary and loading conditions results in the Finite Element approximation of the displacement field, namely $\vec{u}^h$, from which the infinitesimal strain and stress tensors are obtained through the kinematic and constitutive equations, respectively.

Thereby, since the considered case is a pure mode I problem, the respective SIF and Strain Energy Release Rate (SERR) are univocally related through Irwin's relation. As a result, the determination of the SIF may be done through the well-established non-local methods used for numerically computing the SERR. In particular, the present study considered both the axisymmetric particularizations of the SERR approximations as per the G-θ method (Eq. (13)) and the J-Integral (Eq. (14)). For the latter one, the domain integral formulation presented in [25] is used, since, from a numerical point of view, domain integrals usually deliver more accurate results than their path integrals counterparts. In these expressions, the superindex h indicates that the respective magnitude is a numerical approximation of the exact solution, whereas ω represents the elastic strain energy density.

$$G \approx \frac{1}{R+a}\int_{\Omega\setminus\Gamma}\left[\overline{\sigma}^h\cdot\left(\nabla\vec{u}^h\nabla\vec{\theta}^h\right) - \omega^h\mathrm{div}\left(\vec{\theta}^h\right)\right]r\mathrm{d}r\mathrm{d}z \tag{13}$$

$$G \approx \frac{1}{R+a}\int_A\left[(\nabla q)^T\left((\overline{\sigma}^h)^T\frac{\partial\vec{u}^h}{\partial r} - \omega^h\vec{e}_r\right) + \left(\sigma_{\theta\theta}^h\varepsilon_{\theta\theta}^h - \omega^h\right)\frac{q}{r}\right]r\mathrm{d}r\mathrm{d}z \tag{14}$$

In the former method, besides solving the elastic problem, it is required to obtain the vectorial field $\vec{\theta}$, which has to be a piecewise continuously differentiable in Ω, valued $\vec{t}$ at the crack tip ($\vec{t}$ being the unit vector tangent to the crack at its tip), tangent to the crack path in Γ and zero on the boundaries $\partial\Omega$ (except for the edge where the condition of symmetry is applied, where it is forced to be parallel to $\vec{e}_r$). This field was numerically approximated by the solution of a proper variational problem on the discretized domain used for the elastic problem, eventually yielding $\vec{\theta}^h$. It is noteworthy that the differential operators in Eq. (13) are in their axisymmetric form.

Besides, since the expression in Eq. (14) is numerically independent of the integration domain A defined, an annulus centered at the crack tip and with minimum and maximum radii R_{in} and R_{out}, respectively, is used for the sake of simplicity. Besides, q represents a sufficiently smooth scalar field, valued one and zero on the inner and outer circumferences of A, respectively. Per the simple integration domain selected, q was analytically defined.

Given the intrinsic inaccuracy of computing the SIF by means of local approaches relying on the crack tip elastic fields, i.e. stress or displacement, only the two presented non-local methods were used for

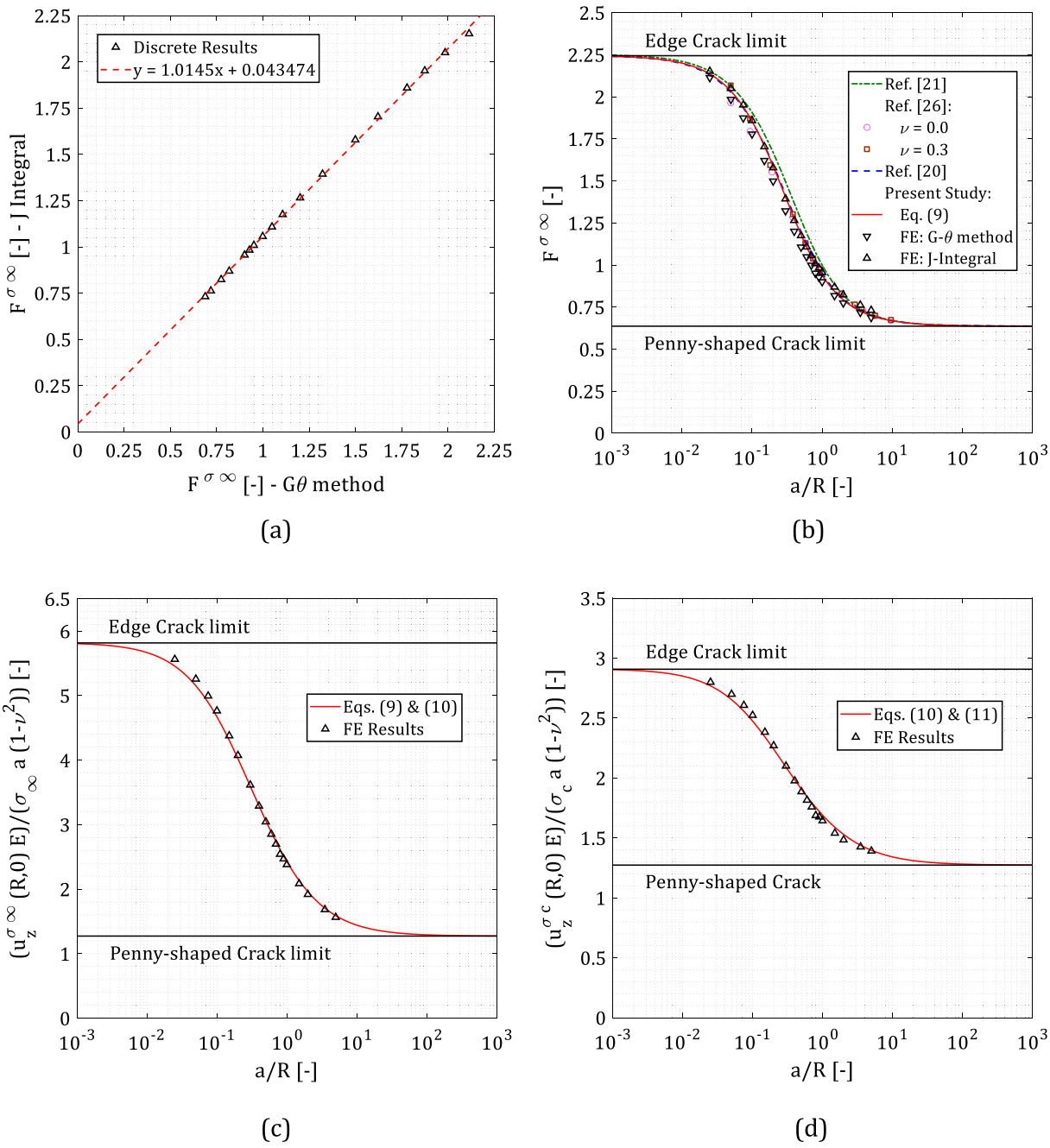

Fig. 4. (a) Correlation of the G-θ method and J-Integral results; (b) Comparison of various SIF models and FE results for the URS scenario; Comparison of the URS (c) and CSL (d) crack opening results for the proposed expressions and FE results.

the verification of the URS loading case. The good correlation obtained between both different predictions shown in Fig. 4 (a) allows proving the representativeness of the numerically computed SIF results. Subsequently, Fig. 4 (b) clearly shows the close matching of numerically obtained SIFs and those by Eq. (9) and references [20,21,26], thus supporting its further use.

For the remaining SIF expressions to be checked against numerical models, i.e. those in Eqs. (10) and (11), crack opening measures are used along with Eq. (12). This poses one main advantage, since the use of displacement-based calculations is more accurate when using Finite Element approximate solutions, and even more when this magnitude is captured far from the singularity.

Since Eq. (9) is already proven accurate, Eq. (10) can be indirectly checked through a comparison between the numerically obtained CMODs in the URS scenario and the predictions delivered through Eq. (12). This is shown in Fig. 4 (c) where the excellent correlation showcased makes it reasonable to conclude that the proposed expression for the SIF in the LLE scenario in Eq. (10) is highly accurate.

Eventually, Eq. (11) may be now numerically checked by using Eq. (12) and the already validated Eq. (10) to yield semi-analytical predictions of the CMOD in the CSL scenario. Note that only the loading conditions are changed in the Finite Element model for this comparison, whose results are shown in Fig. 4 (d). Therein it is clearly seen how the used SIF expressions deliver excellent accuracy with respect to the Finite Element results, thus proving also the correctness of the expression proposed by [20]. Therefore, it is clear that the generalized definition for the annular crack's SIF in Eqs. (5) and (6) can deliver highly representative results for all the cases here considered upon correct choices of m.

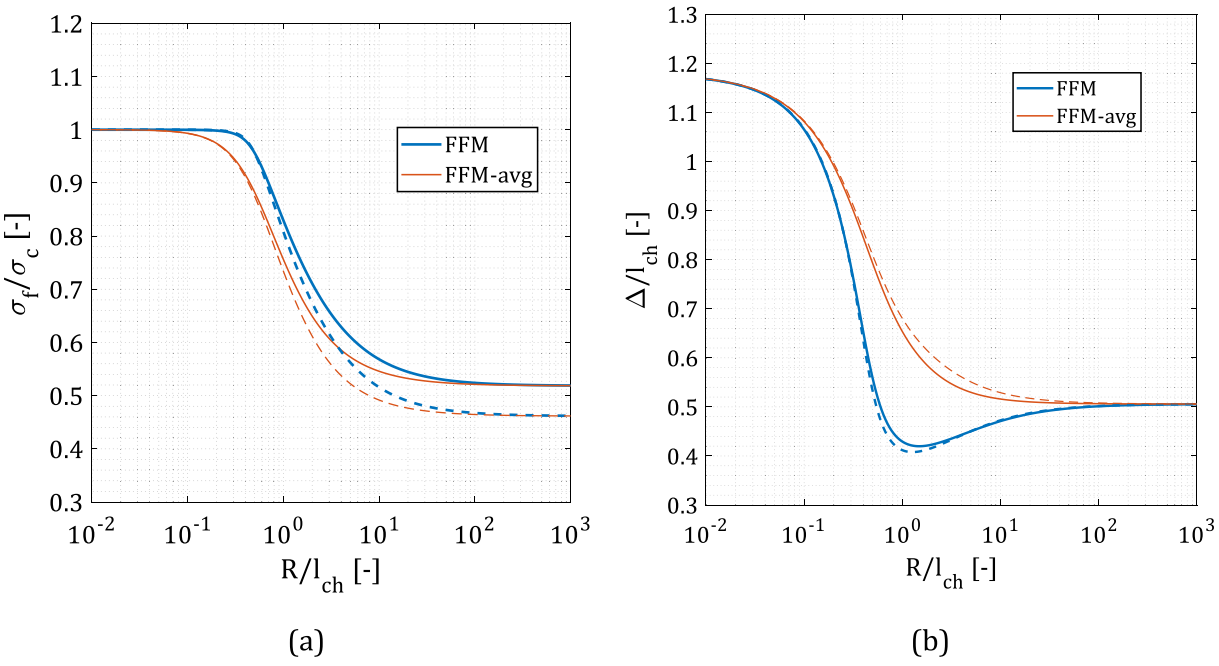

Fig. 5. Comparison of FFM and FFM-avg predictions for $\nu = 0.0$ (solid) and $\nu = 0.5$ (dashed): (a) weakening ratio; (b) finite crack extension. Matching colors/widths imply same method.

Thus, its particularizations into Eqs. (9)–(11) will be hereafter used for the crack onset analysis.

Before proceeding onwards, it is worth noting that the introduction of approximate analytical shape functions greatly simplifies the following analysis. Moreover, the analytical expressions match the limit cases ($R \to 0, \infty$) when Finite Element analyses are vastly difficult to perform. Lastly, the developed formulation inherently considers Poisson's ratio dependence.

3. Finite Fracture Mechanics

According to the FFM framework, crack propagation occurs spontaneously over a finite distance Δ at the minimum loading σ_f in which both the pre-propagation stress field and the energy released upon crack propagation surpass certain thresholds. These are defined, respectively, in terms of the voidless specimen tensile strength σ_c and fracture energy G_c. It is highlighted that, in the present work, σ_c is considered as a structural property towards comprising also materials whose strength is highly flaw-dependent, such as ceramics. On the other hand, σ_c can only be considered as a purely intrinsic material property when the strength flaw-dependence is low, e.g. quasi-brittle materials. Likewise, the Irwiṅs length $l_{ch} = (K_{Ic}/\sigma_c)^2$ shares this nature dependence on the material flaw-sensitiveness.

Moreover, since no plasticity takes place, the crack resistance is independent of the crack length, precluding the material-caused stable crack propagation and thereby causing the complete specimen failure right after crack nucleation should the geometry be positive, i.e. $\partial G/\partial a > 0$.

3.1. Original formulation

According to the FFM formulation by [27], the stress condition requires that, just prior to crack propagation, the crack opening stress σ_{zz} must be higher than σ_c for the whole region where the crack would subsequently propagate, i.e. $\sigma_{zz}(r, \theta, 0) \geq \sigma_c, \forall r \in [R, R + \Delta]$. For cases where $\sigma_{zz}(r)$ is monotonically decreasing, such as the one considered in this work, this condition might be simplified by only enforcing the stress to be higher than σ_c at $r = R + \Delta$. The energy condition states that the energy available for crack growth must be higher than the energy needed to create the new crack surfaces. Besides, the energy balance might be expressed in terms of the SIF through Irwin's relation. The coupled requirements particularized for the annular crack are as shown in Eq. (15).

$$\begin{cases} \sigma_{zz}(R+\Delta) \geq \sigma_c & \text{(a)} \\ \displaystyle\int_0^{\Delta} \left[K_I^{\sigma_\infty}(a)\right]^2 2\pi(a+R)\mathrm{d}a \geq \pi\left[(R+\Delta)^2 - R^2\right]K_{Ic}^2 & \text{(b)} \end{cases} \tag{15}$$

The actual failure stress is then the minimum one such that the two left-hand side terms are larger than the respective right-hand side terms in Eqs. (15). However, since the addressed geometry is positive, the otherwise minimization problem simplifies to a non-linear system of two equations.

Eventually, expanding the expression above and introducing the Irwin's length l_{ch}, it is possible to obtain the ratio of apparent strength reduction due to the presence of the void, σ_f/σ_c, as one of the two unknowns of a determinate system of two nonlinear equations, being the other unknown the spontaneous crack growth Δ.

$$\begin{cases} \dfrac{\sigma_f}{\sigma_c} = \dfrac{1}{1 + \dfrac{4-5\nu}{2(7-5\nu)}\left(\dfrac{R}{R+\Delta}\right)^3 + \dfrac{9}{2(7-5\nu)}\left(\dfrac{R}{R+\Delta}\right)^5} & \text{(a)} \\ \dfrac{\sigma_f}{\sigma_c} = \sqrt{\dfrac{l_{ch}\left(\Delta^2 + 2R\Delta\right)}{2\pi\displaystyle\int_0^{\Delta} a\left(F^{\sigma_\infty}(a)\right)^2(a+R)da}} & \text{(b)} \end{cases} \tag{16}$$

The solution of the integral in the denominator of the energy criterion of Eq. (16b) and the solution of the system of equations in Eqs. (16) is easily performed numerically.

3.2. Averaged stress formulation

The modification introduced in [14] to the original FFM formulation only concerns the stress condition. In this case, it is requested that the resultant force of the crack opening stress over the region where the crack is to propagate should be larger than the critical stress times the

same area. Then, for the axisymmetric case, the stress condition yields Eq. (17).

$$\int_R^{R+\Delta} \sigma_{zz}(r) 2\pi r dr \geq \pi\left[(R+\Delta)^2 - R^2\right]\sigma_c \tag{17}$$

Introducing the stress expression Eq. (1) into Eq. (17), the FFM-avg stress criterion for the annular crack results as in Eq. (18), being the energy criterion still as in Eq. (16b).

$$\frac{\sigma_f}{\sigma_c} = \frac{\Delta^2 + 2\Delta R}{\Delta^2 + 2\Delta R - \frac{4+5\nu}{7-5\nu}\left(\frac{R^3}{R+\Delta} - R^2\right) - \frac{3}{7-5\nu}\left[\frac{R^5}{(R+\Delta)^3} - R^2\right]} \tag{18}$$

The predictions of the weakening ratio σ_f/σ_c by the two FFM criteria are plotted in Fig. 5 (a) in dimensionless form and for the extreme Poisson's ratio values 0.0 and 0.5. As expected, FFM can catch the transition in the weakening ratio from a unit value, for vanishing void sizes, to the inverse of the stress concentration factor (Eq. (2)) for very large pore sizes. While these extreme values are strength-driven only and independent of the FFM variant used, the transition from one another does depend on both the formulation and the fracture toughness (through l_{ch}). As it occurs for other geometries, the FFM-avg model provides lower failure load predictions with respect to the original FFM.

Besides, the results for the dimensionless finite crack extensions Δ/l_{ch} are plotted in Fig. 5 (b), where the extreme values for both FFM formulations respectively coincide at $3\pi/8$ (for $R\to 0$) and $2/1.122^2\pi$ (for $R\to\infty$). In turn, these figures agree with the values of finite crack extension given in the literature for a Penny-shaped Crack [9] and an Edge Crack [14], respectively. They are also coherent with the collapse of the target geometry to these two simpler cases noted in Section 2.1. Besides, it is showcased that the dependency of Δ with the Poisson's ratio ν is small and limited to the transition region between the voidless and large-void solutions.

4. Cohesive Zone Model

In this section, the CZM-based solution is provided in a semi-analytical way, partly as an original contribution, partly to corroborate the FFM approach by a comparison with a well-known and widespread model.

According to the CZM, once a certain threshold on the stress state is reached, the material starts to soften. The region where this cohesive behavior appears is commonly known as process zone, and there the behavior is no longer governed by a stress–strain relation, but by a stress-crack opening dependence. The crack whose length is the stress-free crack plus the process zone is named fictitious crack [28] and, differently to the case of an actual crack, there is no stress singularity at its tip, thus being null its SIF. Eventually, crack nucleation/propagation occurs when the dissipated energy per unit area at the real crack tip is equal to G_c.

In the present study, the simplest CZM model, proposed in [29], is analytically addressed. It considers the cohesive stress constant and equal to σ_c all along the process zone length a_p. Thus, using the superposition principle and enforcing the SIF to vanish at the fictitious crack tip, an equation relating a_p, σ_c and σ_∞ is obtained as in Eq. (19).

$$\sigma_\infty\ F^{\sigma_\infty}(a_p) - \sigma_c\ F^{\sigma_c}(a_p) = 0 \tag{19}$$

The solution to Eq. (19) forces the process zone length a_p to increase as σ_∞ rises. At last, the crack nucleates when the opening displacement at the real crack tip reaches the critical value $\delta_c = G_c/\sigma_c$. Thus, using Eq. (12) and, once again, the superposition principle, the energetic condition of the CZM is as in Eq. (20) (the SIF expressions being given by Eqs. (7)–(11)).

$$2\frac{(1-\nu^2)}{E}\left(\int_0^{a_p} K_I^{\sigma_\infty}\frac{\partial K_I^{\overline{P}}}{\partial \overline{P}}\frac{R+a}{R}da - \int_0^{a_p} K_I^{\sigma_c}\frac{\partial K_I^{\overline{P}}}{\partial \overline{P}}\frac{R+a}{R}da\right) = \frac{G_c}{\sigma_c} \tag{20}$$

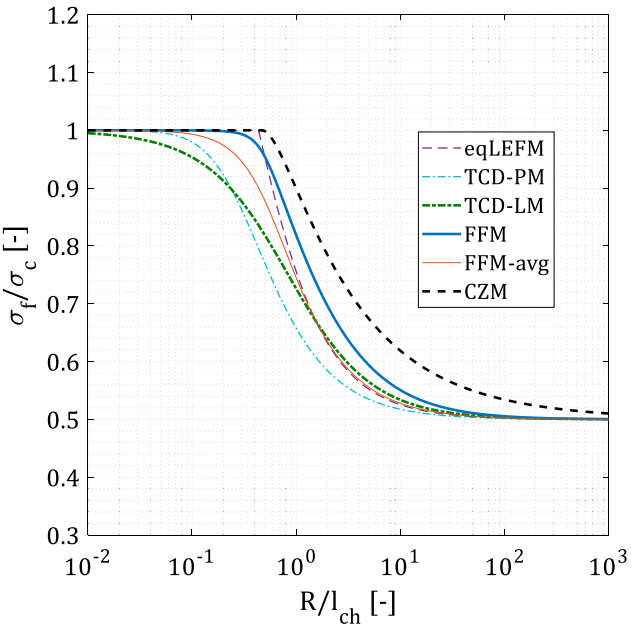

Fig. 6. Comparison of weakening ratio predictions by FFMs, CZM, TCDs, eqLEFM.

Thereby, the CZM failure prediction of the considered specimen is determined by a system of two non-linear equations as in Eqs. (21), easily solvable with numerical algorithms.

$$\begin{cases} \dfrac{\sigma_f}{\sigma_c} = \dfrac{F^{\sigma_c}(a_p)}{F^{\sigma_\infty}(a_p)} & \text{(a)} \\ \dfrac{\sigma_f}{\sigma_c} = \dfrac{l_{ch}R + 2\displaystyle\int_0^{a_p} F^{\sigma_c}F^{\overline{P}}(R+a)da}{2\displaystyle\int_0^{a_p} F^{\sigma_\infty}F^{\overline{P}}(R+a)da} & \text{(b)} \end{cases} \tag{21}$$

It comes naturally to compare this system of equations with those resulting from the FFM analysis. Eq. (21a), which ensures the no stress singularity at the fictitious crack tip, is purely stress-based and, thus, equivalent to the stress criterion used in FFM. On the other hand, Eq. (21b) quantifies the energy dissipated by the process zone at the real crack tip, thereby playing a role similar to the energy criterion of FFM. Moreover, the process zone length a_p represents the CZM's counterpart of the finite crack propagation distance Δ. Therefore, up to a certain extent, both FFM and CZM are equivalent in terms of the quantities they both rely on to predict the crack nucleation. However, there are also some differences: e.g., the stress is not allowed to exceed σ_c in the CZM.

Just as different stress conditions lead to different FFM models, different cohesive laws yield different CZMs [30]. Usually, a good matching is found when comparing Leguillon's FFM with Dugdale CZM for cracked geometries [7,9]. Fig. 6 shows a fairly good agreement between the two models also for the geometry at hand, especially for small void radii; the relative difference is maxed at approximately 12%. On the basis of what showcased in [31] for rhomboidal holes, for low order stress singularities or just stress concentrations as in the present case, an even better match is expected comparing Leguillon's FFM and a CZM with a linear softening law. However, the implementation of other CZM models is beyond the scope of the current work.

5. Simplistic theoretical approaches

Within this section, the solutions provided by simplistic models, namely eqLEFM and TCDs, are described. Although they lack a solid physical background, their simplicity and still relatively good prediction capabilities make them useful for engineering applications.

Table 1
Relevant input parameters used for the comparison with experimental data.

Material	ν	σ_c	K_{Ic}	l_{ch}	Void's radius range
Sodium borosilicate [1]	0.20	82.25 MPa	0.68 MPa$\sqrt{\text{m}}$	68.23 μm	[5.00 – 186.00] μm
Silicon nitride [4]	0.28	735.0 MPa	6.00 MPa$\sqrt{\text{m}}$	66.64 μm	[56.0 – 273.50] μm
Silicon carbide [5]	0.20	58.00 GPa	1.69 MPa$\sqrt{\text{m}}$	8.48 Å	[1.170 –19.960] Å

5.1. Equivalent Linear Elastic Fracture Mechanics

The eqLEFM is a generalization of the conventional LEFM criterion (see e.g. [6]) that allows predicting crack nucleation in uncracked bodies by artificially introducing an initial crack of length a_0. The physical meaning of this length may be different depending on the type of material considered. For highly brittle materials, whose failure is flaw-driven, this length can be regarded as the maximum inherent flaw size, i.e. a structural property. On the other hand, for quasi-brittle materials whose failure is strength-driven, a_0 is a material property.

The ratio of strength reduction due to the spherical void presence according to the eqLEFM is as in Eq. (22), where a_0 has been taken equal to $l_{ch}/(1.122^2\pi)$ and the selection of strength or toughness-driven failure mode is performed by the minimum operator. The factor 1.122 of the toughness-governed failure criterion stands for the SIF's geometry coefficient of an edge crack, which is the geometry to be considered for the very large void size case according to the eqLEFM approach.

$$\frac{\sigma_f}{\sigma_c} = \min\left(\frac{1.122}{F^{\sigma_\infty}\left(l_{ch}/1.122^2\pi, R, \nu\right)}, 1\right) \tag{22}$$

5.2. Theory of Critical Distances

Thoroughly described in [32], the TCD is a set of failure criteria based explicitly on the magnitude of the stress field along a certain fixed length only dependent on the material. This latter amount is determined in order to recover the LEFM solution for the large-crack asymptote, thus implicitly considering the fracture toughness in its formulation, and enabling its use for cases with high gradients or singularities in the stress field. Similarly to the FFM formulation, different TCD variants have been proposed, being the Point Method (TCD-PM) and the Line Method (TCD-LM) the two most frequently used. According to the former, propagation occurs when the stress at a distance of $l_{ch}/2\pi$ from the stress concentration reaches the failure stress σ_c, yielding by Eq. (1) the crack onset stress as in Eq. (23).

$$\frac{\sigma_f}{\sigma_c} = \frac{1}{1 + \frac{4-5\nu}{2(7-5\nu)}\left(\frac{2\pi R}{2\pi R + l_{ch}}\right)^3 + \frac{9}{2(7-5\nu)}\left(\frac{2\pi R}{2\pi R + l_{ch}}\right)^5} \tag{23}$$

In the case of the TCD-LM, the stress field ahead of the stress concentration is averaged over a line of distance $2l_{ch}/\pi$, and failure is considered to happen whenever this measure equals the failure stress σ_c, resulting in Eq. (24).

$$\frac{\sigma_f}{\sigma_c} = \frac{2l_{ch}}{\pi\left\{\frac{2l_{ch}}{\pi} - \frac{(4-5\nu)R^3}{2(14-10\nu)}\frac{(\pi R)^2-(\pi R+2l_{ch})^2}{[R(\pi R+2l_{ch})]^2} - \frac{9R^5}{4(14-10\nu)}\frac{(\pi R)^4-(\pi R+2l_{ch})^4}{[R(\pi R+2l_{ch})]^4}\right\}} \tag{24}$$

The crack onset stress predictions according to the eqLEFM and the TCDs approaches are plotted in Fig. 6 along with the ones previously obtained. It is evident that all the models are able to catch the transition between voidless and large void solutions, although each model provides its own transition: TCD-LM is the one providing the smoother transition, while the most abrupt one is due to eqLEFM. Moreover, TCDs provide the lowest failure stresses, the higher ones being provided by the CZM. Besides, both eqLEFM and CZM coincide in predicting that $R/l_{ch} \approx 0.4$ is the biggest pore for which voidless solutions are valid, i.e. $\sigma_f = \sigma_c$.

6. Comparison with experimental results and atomistic simulations

Along the present section, the FFM approach is validated through experimental data and atomistic simulations available in the literature. For the sake of simplicity, the focus is set only on FFMs because: (i) FFMs represent the main original contribution of the present paper; (ii) the models presented in Section 5 (TCDs and eqLEFM), although easy to achieve, possess a weaker physical background; (iii) it can be easily shown that, for the experimental sets considered, TCD generally provides the poorest predictions; (iv) CZM could match better experimental data if implemented with different cohesive laws as previously observed, but this analysis is beyond the scope of the paper.

Aiming for characterizing the effect that porosity has on the strength of sodium borosilicate specimens, [1] conducted a series of experiments that has then been the reference for many other analytical studies on the topic (e.g. [17,18]). Both porosity and pore sizes were controlled by introducing a certain amount of size-within-a-range nickel spheres during the vacuum hot-pressing of the glass. Per the lack of bonding between the two materials and since the nickel presents a higher thermal coefficient than the borosilicate glass, it is ensured that, from a practical point of view, the matrix will present controlled porosity.

Given the brittleness of borosilicate, specimen failure is flaw-governed and, thus, stochastic. To minimize the scatter, each specimen's surface was equally sanded with SiC grits of 240, 400 and 600, thus generating surface flaws with an approximate size in the range of 8 through 26.5 μm in length. These, in turn, cause the specimen to have a certain flaw insensitivity: superficial defects of a length below a threshold a_0 will have no effect on the effective strength. Then, assuming that these superficial flaws generated by sanding are edge-crack alike, the structural l_{ch} can be estimated as $1.122^2\pi a_0$ (see Section 5.1). For the sake of simplicity, a_0 is taken as the mean value of the sanding-generated flaw sizes, resulting in the value of l_{ch} in Table 1. Eventually, combining the voidless specimen strength reported by the reference and the l_{ch} value in Table 1, the respective average fracture toughness results in $K_{Ic} = 0.68$ MPa$\sqrt{\text{m}}$, which is within the range reported by [33] for different sodium borosilicate compositions, thus supporting the representativeness of the assumptions made.

Thereafter, localized uniaxial tensile conditions were imposed by a four-point bending test. Per the random location of the voids with respect to themselves, to the specimen's surface and to the flaws, higher stress concentrations might arise because of either free-edge effects, void-void, or void-flaw interactions. Added this to the uncertainty in the critical void size, i.e. the one where failure nucleates from, scattering in the experimental results was expected. Since the present investigation addresses single void conditions, only the results respective to the two lowest porosities (2% and 5%, respectively) have been considered and shown in Fig. 7 (a), where both average and extreme cases are reported. For this experimental set, the uncertainty in the vertical axis is considered through the 95% confidence interval of each group of experiments within the same void's radius range, whereas, in the horizontal axis, it is addressed by using the extreme values of each void's radius range.

Good correlation is obtained against analytical predictions, although the experimental scatter hinders determining the most accurate model. Now, considering the average results from the lowest porosity specimens as the most representative case, the best accuracy is provided by FFM-avg. On the other hand, the steep decrease in the apparent strength of the 5% porosity conditions for $R \sim l_{ch}$ infers that there exists non-

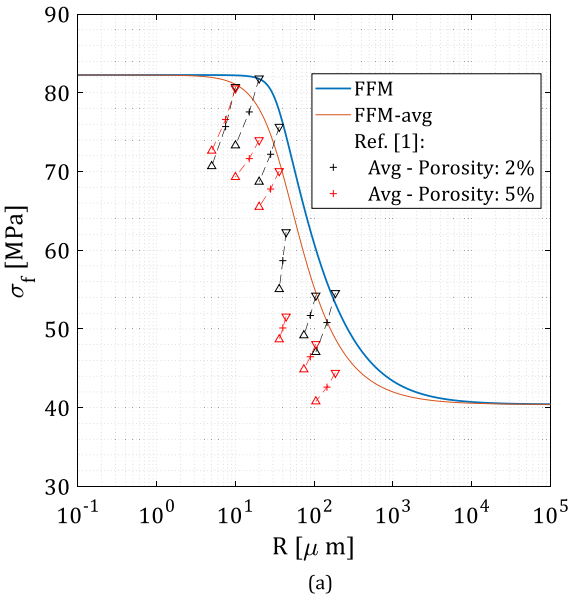

(a)

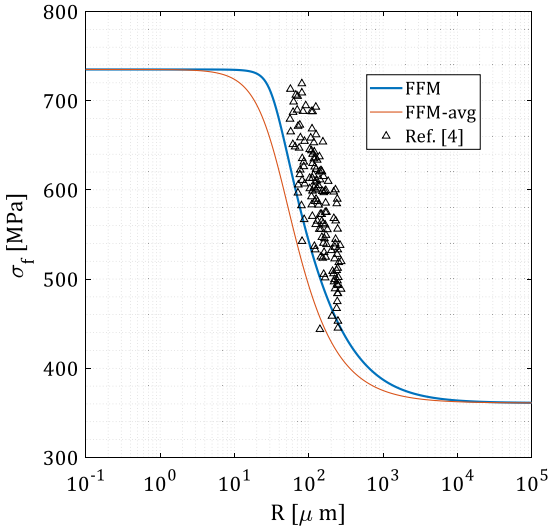

(b)

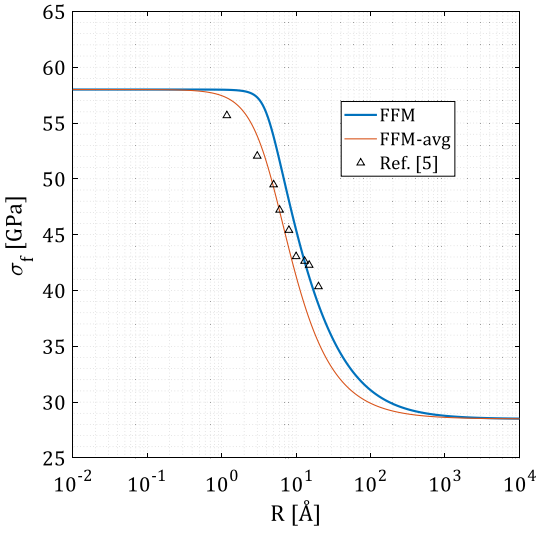

(c)

Fig. 7. Comparison of the different models addressed with: experimental results from (a) [1], (b) [4]; (c) atomistic simulations in [5].

negligible pore interaction in such a case, reducing the representativeness of its results for verification purposes.

Another experimental study on the effect that the presence of spherical pores has on the apparent specimen strength was performed in [4], where the authors generated a single spherical void on silicon nitride specimens. The pore shape, size and location were initially controlled by the introduction of organic inclusions prior to sintering and then double-checked by scanning electron micrographs. This procedure allowed an excellent control of the actual failure conditions, and hence a reduction in the experimental uncertainty.

Being silicon nitride a highly brittle material, its inherent critical flaw size is very small. Nonetheless, per the lack of information concerning each specimen surface finishing, the value of l_{ch} used for the experimental comparison in Fig. 7 (b) was computed out of the tensile strength and fracture toughness provided by the authors and reported in Table 1. It is evident that the analytical predictions lie on the left side of experimental data set. However, as already discussed, the surface finishing might affect the specimen flaw sensitiveness by raising l_{ch} (the value in Table 1 is regarded as a lower bound). Hence, the shift can be explained by a larger structural length that would move the analytical predictions rightwards. What is not changing with the considered l_{ch} is the mean slope of the failure stress vs. the hole radius, which is truly well fitted by the FFM approaches. Hence, the representativeness of these formulations is inferred also from comparison with this second data set.

Despite the relatively good agreement in the results obtained with both previous experimental data sets, it is seen that the existence of flaws in highly flaw-sensitive materials (and so, the proper determination of l_{ch}) hinders a bold conclusion to be made regarding the soundness of the FFM approach. To sort out this handicap, either a material with a perfect internal structure or a more flaw tolerant material should be used. Concerning the former option, since it is not possible to obtain crystalline structures without flaws at temperatures above 0 K, the only way of characterizing the purely material failure is via atomistic simulations, such as those performed in [5].

In their study, Ippolito and co-workers [5] explicitly modelled a β-Silicon carbide crystalline lattice, and the spherical void was created by removing certain atoms from the atomic pattern. Therein it was found that, whenever the external dimension of the virtual specimen was at least ten times bigger than the voids radius, free-edge effects were negligible. Moreover, values for the strength and fracture toughness of the atomistic arrange were computed from bespoke simulations, allowing to directly determine the Irwin's length as $l_{ch} = (K_{Ic}/\sigma_c)^2$ and yielding the values reported in Table 1. Notice that by eliminating the intrinsic defects of a real crystalline lattice, the values of the strength (Irwin's length) are several orders of magnitude higher (lower) than those obtained macroscopically. It is highlighted that this conclusion is in accordance to the original findings of Griffith in [34] on the large difference in the breaking load of the bulk glass in comparison with the theoretical load required for breaking the atomic bonds.

Per the microscopic arrangements of the atomistic pattern, some roughness in the voids surface is showcased, especially noticeable for small void's radii. However, since the absolute upper bound in the length of these irregularities, equal to the interatomic distance $c_0 = 2.64$ Å, is of the same order than the material's flaw sensitiveness $a_0 = l_{ch}/(1.122^2\pi)$, their effect was not further considered. Subsequently, the comparison conducted in Fig. 7 (c) between these simulations and the herein discussed analytical models shows a great correlation, especially when considering the FFM formulation in its average stress variant. Note that excellent correlation between molecular dynamics simulations and FFM has already been noticed for different flaw shapes in previous studies such as that in [35].

7. Conclusions

The tensile failure of a linear elastic and brittle material containing a spherical cavity is thoroughly investigated within this study. Although

presenting a non-singular stress field, the maximum stress criterion is not deemed suitable since it does not capture the experimentally observed size effect on the voided specimen weakening. However, this scaling effect is caught by more refined approaches that take energy balances and/or energy quantities into account. Among these formulations, the most representative ones (and those herein presented) are Finite Fracture Mechanics, Cohesive Zone Model, Theory of Critical Distances and equivalent LEFM.

Since the energy considerations of the used approaches (except for Theory of Critical Distances) can be accounted for through the Stress Intensity Factor of the prospective crack, extensive characterization of the annular crack stemming from the void's equator is conducted. In particular, a general procedure for obtaining the annular crack SIF under different loading conditions has been proposed and checked against Finite Element results, showing an excellent accuracy and even holding for loading cases not previously considered.

The obtention of these approximated SIF functions, combined with the well-known solution for the spherical void's stress field, allows for the derivation of semi-analytical expressions for failure per different approaches. It is noteworthy the use of Paris' equation to deal with the CZM analytically.

As expected, the adoption of energy considerations allows obtaining the gradual transition from the stress-driven extreme solutions, namely large-void and voidless. Although each theory provides a slightly different prediction, all of them agree to place the transition within the void's radius range ($0.1\ l_{ch}, 10\ l_{ch}$). Moreover, the showcased relative differences in the failure prediction curves yielded by the different theories considered are consistent with those observed in the literature for different stress concentrations.

Eventually, the comparison with two sets of experimental data and one set of atomistic simulations on ceramic brittle materials proves the representativeness of the considered approaches, especially those comprised within the FFM framework. Given the intrinsic scatter and uncertainty in the experimental sets, the obtention of a bold conclusion on the most accurate theory is hindered, both the FFM approaches providing reasonable accuracy. The data scattering due to the presence of flaws is eliminated in the atomistic simulations: in such a case FFM-avg provides the most accurate predictions.

CRediT authorship contribution statement

A. Chao Correas: Conceptualization, Software, Writing – original draft, Visualization. **M. Corrado:** Conceptualization, Writing – review & editing. **A. Sapora:** Conceptualization, Writing – review & editing. **P. Cornetti:** Conceptualization, Writing – review & editing, Supervision.

Declaration of Competing Interest

The authors declare that they have no known competing financial interests or personal relationships that could have appeared to influence the work reported in this paper.

Acknowledgements

This project has received funding from the European Union's Horizon 2020 research and innovation programme under the Marie Skłodowska-Curie grant agreement No 861061.

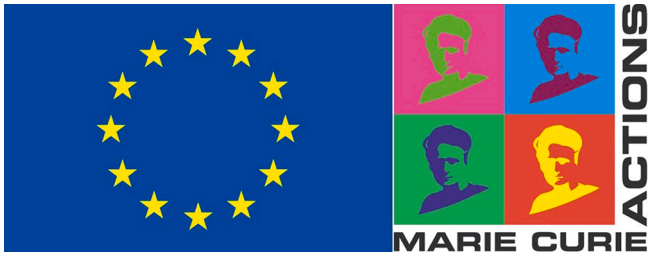

References

[1] R.L. Bertolotti, R.M. Fulrath, Effect of micromechanical stress cocentrations on strength of porous glass, J. Am. Ceram. Soc. 50 (11) (1967) 558–562, https://doi.org/10.1111/j.1151-2916.1967.tb14998.x.
[2] B. ZHAO, T. YU, W. DING, X. LI, Effects of pore structure and distribution on strength of porous Cu-Sn-Ti alumina composites, Chinese J. Aeronaut. 30 (6) (2017) 2004–2015, https://doi.org/10.1016/j.cja.2017.08.008.
[3] J.N. Goodier, Concentration of stress around spherical and cylindrical inclusions and flaws, J. Appl. Mech. 55 (1933) 39–44.
[4] M. Kaji, S. Yoshiura, M. Nishimura, Strength estimation for silicon nitride specimens with a spherical void, J. Mater. Sci. 29 (22) (1994) 5947–5952, https://doi.org/10.1007/BF00366879.
[5] M. Ippolito, A. Mattoni, N. Pugno, L. Colombo, Failure strength of brittle materials containing nanovoids, Phys. Rev. B - Condens. Matter Mater. Phys. 75 (2007) 1–7, https://doi.org/10.1103/PhysRevB.75.224110.
[6] Z.P. Bažant, Scaling of Structural Strength, Elsevier, Amsterdam, 2005. https://doi.org/10.1016/B978-0-7506-6849-1.X5000-7.
[7] P. Cornetti, A. Sapora, A. Carpinteri, Short cracks and V-notches: finite fracture mechanics vs. cohesive crack model, Eng. Fract. Mech. 168 (2016) 2–12, https://doi.org/10.1016/j.engfracmech.2015.12.016.
[8] A. Sapora, P. Cornetti, A. Campagnolo, G. Meneghetti, Fatigue limit: crack and notch sensitivity by finite fracture mechanics, Theor. Appl. Fract. Mech. 105 (2020) 102407, https://doi.org/10.1016/j.tafmec.2019.102407.
[9] P. Cornetti, A. Sapora, Penny-shaped cracks by finite fracture mechanics, Int. J. Fract. 219 (1) (2019) 153–159, https://doi.org/10.1007/s10704-019-00383-9.
[10] D. Leguillon, R. Piat, Fracture of porous materials - Influence of the pore size, Eng. Fract. Mech. 75 (7) (2008) 1840–1853, https://doi.org/10.1016/j.engfracmech.2006.12.002.
[11] P.P. Camanho, G.H. Erçin, G. Catalanotti, S. Mahdi, P. Linde, A finite fracture mechanics model for the prediction of the open-hole strength of composite laminates, Compos. Part A Appl. Sci. Manuf. 43 (8) (2012) 1219–1225, https://doi.org/10.1016/j.compositesa:2012.03.004.
[12] E. Martin, D. Leguillon, N. Carrère, A coupled strength and toughness criterion for the prediction of the open hole tensile strength of a composite plate, Int. J. Solids Struct. 49 (26) (2012) 3915–3922, https://doi.org/10.1016/j.ijsolstr.2012.08.020.
[13] A. Sapora, P. Cornetti, Crack onset and propagation stability from a circular hole under biaxial loading, Int. J. Fract. 214 (1) (2018) 97–104, https://doi.org/10.1007/s10704-018-0315-6.
[14] P. Cornetti, N. Pugno, A. Carpinteri, D. Taylor, Finite fracture mechanics: a coupled stress and energy failure criterion, Eng. Fract. Mech. 73 (14) (2006) 2021–2033, https://doi.org/10.1016/j.engfracmech.2006.03.010.
[15] A. Doitrand, R. Henry, S. Meille, Brittle material strength and fracture toughness estimation from four-point bending test, J. Theor. Comput. Appl. Mech. (2021) 1–17. https://doi.org/10.46298/jtcam.6753.
[16] A.G. Evans, D.R. Biswas, R.M. Fulrath, Some effects of cavities on the fracture of ceramics: II, Spherical cavities, J. Am. Ceram. Soc. 62 (1-2) (1979) 101–106, https://doi.org/10.1111/j.1151-2916.1979.tb18815.x.
[17] V.D. Krstic, Fracture of brittle solids in the presence of a spherical cavity, Acta Metall. 33 (3) (1985) 521–526, https://doi.org/10.1016/0001-6160(85)90094-X.
[18] V.D. Krstic, Effect of microstructure on fracture of brittle materials: unified approach, Theor. Appl. Fract. Mech. 45 (3) (2006) 212–226, https://doi.org/10.1016/j.tafmec.2006.03.005.
[19] A. Sapora, A.R. Torabi, S. Etesam, P. Cornetti, Finite fracture mechanics crack initiation from a circular hole, Fatigue Fract. Eng. Mater. Struct. 41 (7) (2018) 1627–1636, https://doi.org/10.1111/ffe.v41.710.1111/ffe.12801.
[20] T. Fett, Stress intensity factors and weight function for a void with an annular crack, Int. J. Fract. 67 (2) (1994) R41–R47, https://doi.org/10.1007/BF00019608.
[21] D.J. Green, Stress intensity factor estimates for annular cracks at spherical voids, J. Am. Ceram. Soc. 63 (5-6) (1980) 342–344, https://doi.org/10.1111/jace:1980.63.issue-5-610.1111/j.1151-2916.1980.tb10737.x.
[22] H. Tada, P.C. Paris, G.R. Irwin, The Stress Analysis of Cracks Handbook, Third Edition, ASME Press, 2000. https://doi.org/10.1115/1.801535.
[23] P.C. Paris, The Mechanics of Fracture Propagations and Solutions to Fracture Arrester Problems - Document D2-2195, Boeing Co. (1957).
[24] M.S. Alnæs, J. Blechta, J. Hake, A. Johansson, B. Kehlet, A. Logg, C. Richardson, J. Ring, E. Rognes, G.N. Wells, The FEniCS Project Version 1.5, Arch. Numer. Softw. 3 (2015) 9–23. https://doi.org/https://doi.org/10.11588/ans.2015.100.20553.
[25] R. Nahta, B. Moran, Domain integrals for axisymmetric interface crack problems, Int. J. Solids Struct. 30 (15) (1993) 2027–2040, https://doi.org/10.1016/0020-7683(93)90049-D.
[26] Y. Murakami, T. Norikura, T. Yasuda, Stress Intensity Factors for a Penny-Shaped Crack Emanating from an Ellipsoidal Cavity回転だ円体空かから発生した円板状き裂の応力拡大係数, Trans. Japan Soc. Mech. Eng. Ser. A. 48 (436) (1982) 1558–1565, https://doi.org/10.1299/kikaia.48.1558.
[27] D. Leguillon, Strength or toughness? A criterion for crack onset at a notch, Eur. J. Mech. A/Solids. 21 (1) (2002) 61–72, https://doi.org/10.1016/S0997-7538(01)01184-6.
[28] A. Hillerborg, M. Modéer, P.-E. Petersson, Analysis of crack formation and crack growth in concrete by means of fracture mechanics and finite elements, Cem. Concr. Res. 6 (6) (1976) 773–781, https://doi.org/10.1016/0008-8846(76)90007-7.
[29] D.S. Dugdale, Yielding of steel sheets containing slits, J. Mech. Phys. Solids. 8 (1960) 100–104. https://doi.org/10.1016/0022-5096(60)90013-2.

[30] P. Cornetti, M. Muñoz-Reja, A. Sapora, A. Carpinteri, Finite fracture mechanics and cohesive crack model: weight functions vs. cohesive laws, Int. J. Solids Struct. 156–157 (2019) 126–136, https://doi.org/10.1016/j.ijsolstr.2018.08.003.
[31] A. Doitrand, R. Estevez, D. Leguillon, Comparison between cohesive zone and coupled criterion modeling of crack initiation in rhombus hole specimens under quasi-static compression, Theor. Appl. Fract. Mech. 99 (2019) 51–59, https://doi.org/10.1016/j.tafmec.2018.11.007.
[32] D. Taylor, The Theory of Critical Distances, Elsevier, Amsterdam, 2007. https://doi.org/10.1016/B978-0-08-044478-9.X5000-5.
[33] M. Barlet, J.-M. Delaye, T. Charpentier, M. Gennisson, D. Bonamy, T. Rouxel, C. L. Rountree, Hardness and toughness of sodium borosilicate glasses via Vickers's indentations, J. Non. Cryst. Solids. 417–418 (2015) 66–79, https://doi.org/10.1016/j.jnoncrysol.2015.02.005.
[34] A.A. Griffith, VI. The phenomena of rupture and flow in solids, Philos. Trans. R. Soc. London. Ser. A, Contain. Pap. a Math. or Phys. Character. 221 (1921) 163–198. https://doi.org/10.1098/rsta.1921.0006.
[35] L. Brochard, I.G. Tejada, K. Sab, From yield to fracture, failure initiation captured by molecular simulation, J. Mech. Phys. Solids. 95 (2016) 632–646, https://doi.org/10.1016/j.jmps.2016.05.005.